Proceedings of the International Conference
Nanomaterials: Applications and Properties
Vol. **4** No 1, 01NTF05(6pp) (2015)

Grazing-incidence Small-angle X-ray Scattering Technique for Probing Nanostructures and Processes at Nanoscale

M. Jergel[1,*], P. Šiffalovič[1], K. Végsö[1], E. Majková[1], S.V. Roth[2], O. Konovalov[3], H.Y. Lee[4]

[1] *Institute of Physics, Slovak Academy of Sciences, Dúbravská cesta 9., 845 11 Bratislava, Slovakia*
[2] *HASYLAB/DESY, Notkestrasse 86, 22603 Hamburg, Germany*
[3] *European Synchrotron Radiation Facility, BP 220, 38043 Grenoble, France*
[4] *National Synchrotron Radiation Research Center, 101 Hsin-Ann Road, Hsinchu 30076, Taiwan*

(Received 03 June; published online 29 August 2015)

The paper presents the grazing-incidence small-angle X-ray scattering technique and its application to the studies of self-assembly and re-assembly effects of colloidal nanoparticles. Two basic cases are exemplified - solvent evaporation driven self-assembly and self-assembly driven by barrier movement in the Langmuir-Blodgett trough. Studies of the nanoparticle re-assembly effects due to the surfactant removal complete the overview. These examples document strength of GISAXS for an *in situ* tracking of processes at nanoscale. The results have direct implications for tailored preparation of the self-assembled nanoparticle templates for sensing, plasmonics and other applications.

Keywords: GISAXS, X-rays, Nanoparticle, Self-assembly, Langmuir-Blodgett, Drop casting.

PACS numbers: 61.05.Cf, 68.18.Fg, 68.47.Pe

1. GRAZING-INCIDENCE SMALL-ANGLE X-RAY SCATTERING

The grazing-incidence small-angle X-ray scattering (GISAXS) is a unique technique for non-destructive characterization of nanostructures and *in situ* probing of processes at nanoscale [1-3]. The basic scheme of GISAXS experiment is shown in Fig. 1.

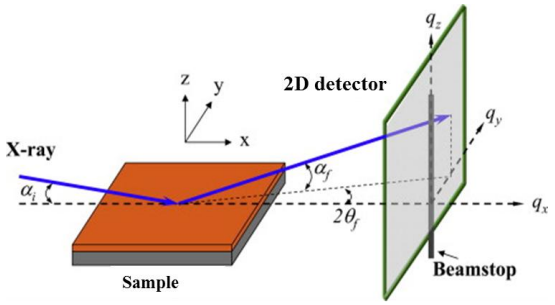

Fig. 1 – Scheme of a GISAXS experiment

The GISAXS is a reflection-mode counterpart of the small-angle X-ray scattering (SAXS) measured in the transmission mode. The monochromatic X-ray beam (usually CuK_α line, 8027 eV) impinges on a planar sample surface under a small angle of incidence above the critical value for the total external reflection, being scattered by any inhomogeneities of electron density on the surface or below in a depth controlled by the angle of incidence. These can be *e.g.* nanoparticles on the substrate or clusters below the surface. The scattered intensity is projected onto a 2-dimensional (2D) detector placed normal to the plane of incidence (GISAXS pattern). Within the first Born (kinematical) approximation of the wave equation describing the scattering process, which is valid for the incidence angles ≈3 times larger than the critical value, the GISAXS pattern is directly proportional to the Fourier transform of the electron density autocorrelation function in real space. In the case of periodic arrangement of scattering entities, the GISAXS pattern is a product of the interference function describing the periodicity and controlling positions of the GISAXS peaks, and the form factor of the entities, *e.g.* nanoparticles, that controls intensity of the GISAXS peaks. Hence, the GISAXS pattern provides indirect information on the nanoparticle shape and order that can be retrieved by GISAXS simulation within an appropriate model. On the other hand, some parameters such as the interparticle distance or size of the coherently scattering domains can be obtained directly. The maximum resolution of laboratory GISAXS devices expressed in real space reaches 100 nm, however, resolution up to 1 μm or more may be achieved with highly collimated synchrotron beams. The Fig. 2 shows a SAXS/GISAXS Nanostar device (Bruker AXS) with high-intense Ga liquid-metal jet anode source (Excillum) installed at the Institute of Physics SAS.

Fig. 2 – Nanostar device with Excillum source

Comparing with direct space imaging local methods such as electron microscopy or scanning probe techniques, the information provided by GISAXS is inherently statistical, being averaged over the whole irradiated volume. Other GISAXS advantages are non-destructive character of the sample probing and no

* matej.jergel@savba.sk

need for vacuum. Therefore GISAXS is suitable for *in situ* tracking the processes at nanoscale including the air/water interfaces where other techniques fail due to the high vapour pressure and surface tension of water. Hence, GISAXS is a method of choice *e.g.* for studies of self-assembly effects of colloidal nanoparticles as it will be demonstrated in the following.

2. SELF-ASSEMBLED NANOPARTICLE ARRAYS

Highly monodisperse nanoparticles exhibit spontaneous self-assembly into large arrays which provides an effective way to prepare regular macroscopic nanoparticle monolayers and multilayers by Langmuir-Blodgett and Langmuir–Schaefer techniques or 3D nanoparticle arrays by solution drop casting followed by solvent evaporation [4]. Colloidal metallic nanoparticle self-assemblies are applied in electrical strain gauges with tunneling regime of electrical conductivity that outperforms conventional metal film-based strain gauges. Semiconducting metal oxide nanoparticle films represent an ideal platform for gas sensing due to a significantly enhanced surface/volume ratio with applications in civil security and health care. Self-assemblies of plasmonic nanoparticles are attractive as templates for the surface-enhanced Raman scattering studies. Self-assembled templates of polystyrene nanoparticles are used in lift-off lithography.

In order to tailor properties of the nanoparticle arrays for envisaged applications, knowledge of the details of the self-assembly process is essential and must be studied. Here, GISAXS proves to be an excellent method for tracking the nanoparticle ordering at nanoscale during the self-assembly process. Alternatively, it may be combined with measurements of macroscopic physical quantities such as the surface pressure, refractive index or surface potential to get a complex picture of the process. In the examples to follow, the solvent evaporation driven self-assembly after the nanoparticle colloidal solution drop casting on a substrate and a modified Langmuir–Schaefer deposition [5] were employed. In the latter case, a drop of colloidal nanoparticle solution was applied and spread on the water surface in a Langmuir-Blodgett trough. A controlled barrier movement reduced gradually the surface area which resulted in the formation of a closed self-assembled nanoparticle monolayer at the air/water interface, actually the nanoparticle Langmuir film in analogy to traditional molecular Langmuir film. The film was transferred onto the substrate by a controlled removal of the water subphase.

3. GISAXS STUDIES OF NANOPARTICLE SELF-ASSEMBLY AND RE-ASSEMBLY

3.1 Example 1 - Solvent Evaporation Driven Self-assembly

The colloidal iron oxide nanoparticles of 6.4±0.6 nm diameter dispersed in toluene were used. The surfactant shell of oleic acid and oleylamine prevented from the nanoparticle aggregation. The GISAXS experiments were conducted at BW4 beamline, HASYLAB/DESY Hamburg. A 5 μL drop of colloidal nanoparticles was applied onto a clean silicon substrate at room temperature. Two alignments of the probing X-ray beam with respect to the substrate surface were employed. In the case of a nearly parallel alignment (0.1 degree deviation) and the substrate slightly shifted down, GISAXS was able to distinguish between the nanoparticle self-assembly in the colloidal drop volume (Fig. 3 top) and at the drop surface (Fig. 3 center). In the latter case, a narrow streak in the GISAXS pattern slightly inclined with respect to the q_z axis (normal to the substrate component of the scattering vector) is visible in the moment when the X-ray beam intersects receding surface of the drying drop. On the solvent evaporation (Fig. 3 bottom), all nanoparticles are on the substrate outside the X-ray beam and no scattering is observed.

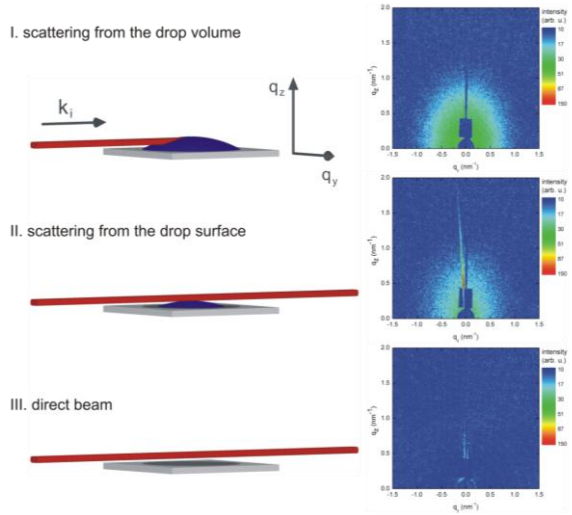

Fig. 3 - Scheme of the drying colloidal drop (left) and the corresponding GISAXS patterns taken *in situ* (right) in the nearly parallel mode

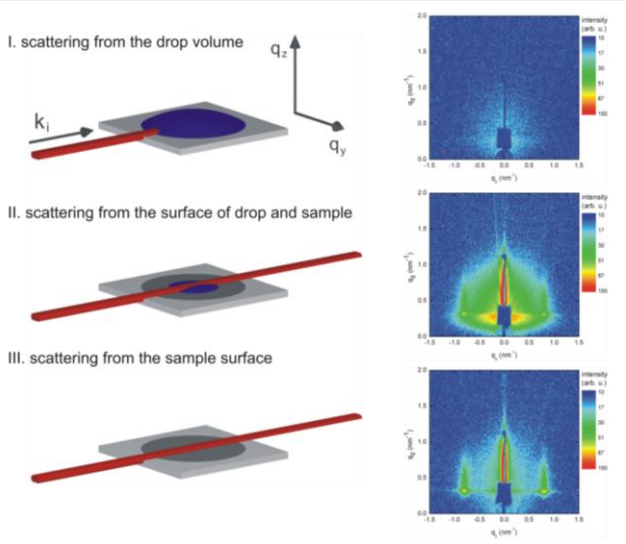

Fig. 4 – Scheme of the drying colloidal drop (left) and the corresponding GISAXS patterns taken *in situ* (right) in the inclined mode

In the case of the inclined alignment of the X-ray beam (0.18 degree incidence angle), GISAXS absorbed at first strongly by the volume of the colloidal drop

(Fig. 4 top) gradually emerges as the solvent evaporates (Fig. 4 center) and finally distinct side maxima in the GISAXS pattern (Fig. 4 bottom) prove the nanoparticle self-assembly into a regular array after the complete solvent evaporation. This is a clear difference in comparison with Fig. 3 top which could be simulated with the form-factor function of a single spherical nanoparticle and a constant interference function. Hence, no positive evidence of the nanoparticle self-assembly inside the colloidal drop (liquid phase) was found.

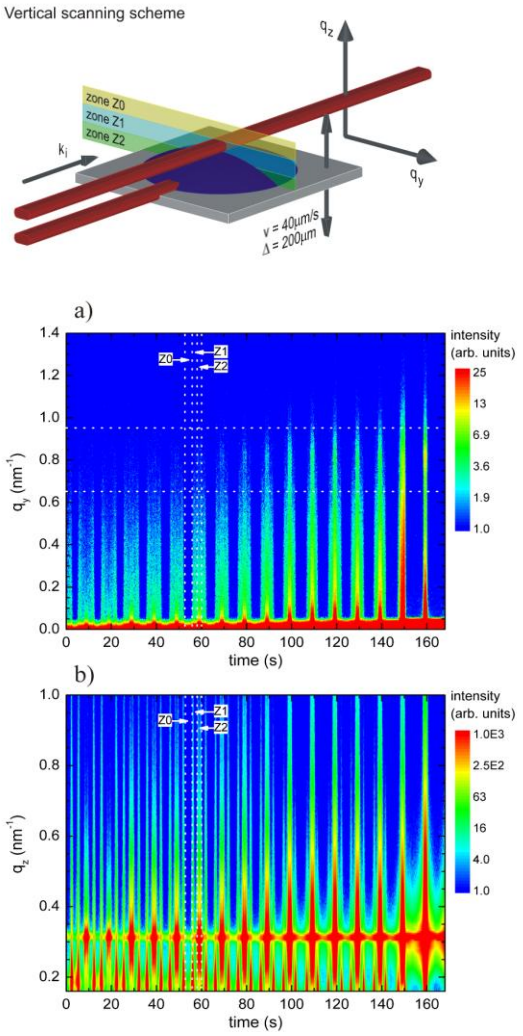

Fig. 5 – Scheme of the vertical oscillations of the sample stage and temporal evolution of the selected lateral and normal cuts of the GISAXS patterns taken *in situ* during oscillations

In order to locate the self-assembly region, vertical and horizontal oscillations of the sample stage were added and separately applied during the drop drying. The scanning velocity was adapted to the exposure and read-out times of the 2D detector in order to minimize the effect of the spatial smearing. In this way, it was possible to collect a large number of GISAXS patterns from different evaporation stages of the drying colloidal drop. An example for vertical oscillations is shown in Fig. 5 along with temporal evolution of the lateral (in-plane) q_y cuts and normal q_z cuts of the GISAXS pattern at the critical angle and at $q_y = 0$, respectively. During one oscillation cycle, one can distinguish between three types of the X-ray scattering from the drying drop that correspond to the zones in real space labelled as Z0, Z1 and Z2. The experimentally relevant zones Z1 and Z2 can be attributed to the scattering from the drying drop surface and volume, respectively. Similarly to Fig. 3 center, a strong scattering streak occurs due to the X-ray scattering from the drop surface when the beam passes from zone Z0 to Z1. No nanoparticle self-assembly such as that manifested by the side maxima in Fig. 4 bottom can be identified when the X-ray beam enters zone 2, in accord with Fig. 3 top.

A similar analysis was performed with horizontal oscillations of the sample stage. Relating the information on the temporal evolution of the GISAXS signal to its spatial distribution at respective times, the three-phase interface represented by the shrinking contour line of the drying drop was finally identified as the region of the nanoparticle self-assembly.

3.2 Example 2 - Self-assembly at Water/Air Interface

While the solvent-evaporation driven self-assembly provides rather small nanoparticle arrays limited by the size of the drying drop, large and homogenous arrays of self-assembled nanoparticles can be prepared as Langmuir films at the air/water interface. A chlorophorm solution of colloidal Ag nanoparticles of 7.0±0.7 nm diameter (concentration of 0.2 mg/mL) was applied by a microsyringe on the water surface between barriers in a Langmuir-Blodgett trough. After spreading the nanoparticles at the air/water interface, the solvent was let to evaporate for 15 minutes before the measurement. The *in situ* GISAXS measurements were performed at ID10B beamline at ERSF, Grenoble. In particular, a continuous series of the GISAXS patterns was recorded as a movie during the nanoparticle Langmuir film compression and expansion at a constant barrier speed of 26 cm^2/min. The time between the two successive patterns of 1.87 s was short enough not to miss any relaxation effect. The surface pressure controlled by the barrier movement was measured simultaneously by the Wilhelmy plate. Hence, immediate response of the nanoparticle self-assembly driven by the barrier movement to the changing surface pressure could be measured and intermediate phases far from equilibrium detected.

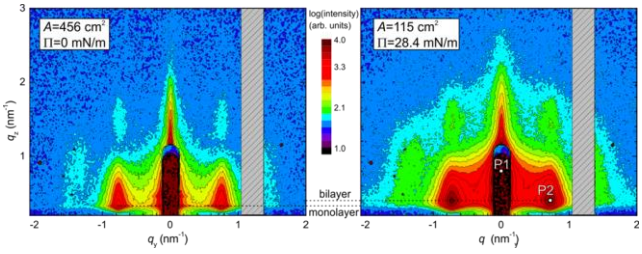

Fig. 6 – GISAXS patterns before(left) and after (right) the compression

The Fig. 6 shows the GISAXS patterns of the nanoparticle Langmuir film before and after the compression. The q_z and q_y are the normal and lateral (along the air/water interface) scattering vector components. The distinct side maxima running along q_z, called also Bragg rods, suggest presence of an ordered nanoparticle mono-

layer from the very beginning while the null ellipsometry image measured separately (Fig. 7 right) shows that this monolayer is discontinuous at small surface pressure. Considering the monolayer islands as hexagonally ordered close-packed 2D crystals of spherical nanoparticles, the lattice spacing before compression reads $d_{10} = 2\pi/q_{y,1B}$ which for the first Bragg rod maximum position $q_{y,1B} = 0.75$ nm^{-1} gives the nearest-neighbour interparticle distance $\Delta = 2d_{10}/\sqrt{3} = 9.7$ nm. The compression results in an intensity redistribution along q_y of the central (at $q_z = 0$) and the first Bragg rods (Fig. 6). On the former, the maximum intensity shifts from the critical exit angle (so called Yoneda peak) to peak P1 (hidden by the specular beam stop to prevent detector damage) after compression which indicates the nanoparticle layering. On the latter, peak P2 evolves at the position that suggests formation of a vertically correlated second layer, namely the hexagonal close-packed bilayer [6].

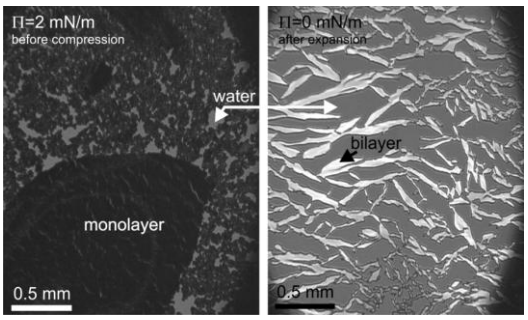

Fig. 7 – Null ellipsometry images of the nanoparticle Langmuir film before compression (right) and after expansion (left)

Based on the simultaneously measured pressure–area isotherm and GISAXS patterns, four principal stages of the nanoparticle Langmuir film compression can be identified (Fig. 8). In stage I, no measureable change in the surface pressure Π is detected (Fig. 8a). The self-assembly of nanoparticles evidenced by the presence of Bragg rods in GISAXS (Fig. 6) and occuring within isolated self-assembled nanoparticle islands (Fig. 7 right) is observed. The surface elastic modulus E calculated from Π derivative (Fig. 8a) has no physical meaning for the freely floating isolated islands here. Presumably, the nanoparticle islands coalesce gradually into larger assemblies with increasing surface pressure. The reduction of the Bragg rod width (Fig. 8c) is not observed because of the limited size of the coherently scattering domains restricted by the nanoparticle cumulative disorder in the pristine islands. In stage II, a steady increase in the surface pressure and elastic modulus is observed (Fig. 8a) as the proceeding island coalescence gets gradually the larger assemblies into contact. This accumulates stress at the assembly boundaries that is relieved by the nanoparticle rearrangements into a close-packed monolayer.

A nearly unchanged Bragg rod maximum position and width (Fig. 8b,c) suggest that the local hexagonal order from the original islands is preserved. The nanoparticle Langmuir film at the end of stage II is completely closed, being suitable for the transfer onto a solid substrate to deposit a high-quality nanoparticle

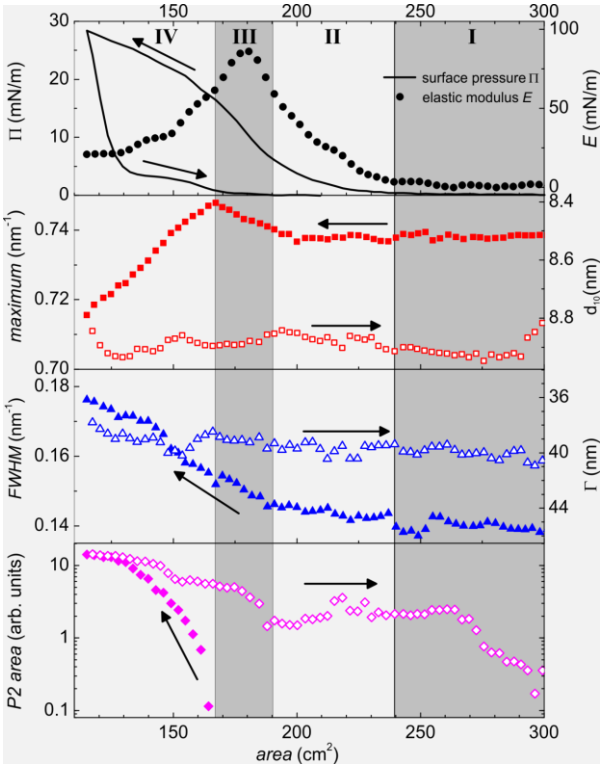

Fig. 8 – The major compression stages of the nanoparticle Langmuir film. The arrows show the compression and expansion periods.

monolayer. In stage III, a steeper increase in the surface pressure followed by a maximum in the surface elastic modulus preceding a bilayer formation is observed. A shift in the Bragg rod maximum position to higher q_y values suggests a decrease in the lattice spacing d_{10} by ≈0.1 nm (Fig. 8b) while a simultaneous increase in the Bragg rod width (Fig. 8c) indicates a deterioration of the nanoparticle order due to the accumulated stress. Such a Bragg rod behaviour can be explained by a slight compressive deformation of the polymer surfactant capping of the nanoparticles (oleylamin and oleic acid). This transient compression phase was not observed in the experiments under steady-state conditions. In stage IV, the peak P2 indicates a newly formed vertically correlated second nanoparticle layer allowing stress relief which results in the reversed shift of the Bragg rod maximum position and increase in the d_{10} lattice spacing. The Bragg rod width increases as well suggesting growing disorder. Such a simultaneous growth of the lattice spacing and disorder is typical for the paracrystal model [7]. The Bragg rod maximum position and width are not recovered during the film expansion, suggesting a stable nanoparticle order in the bilayer. These results have direct implications for preparation of large-area high-quality nanoparticle arrays.

3.3 Example 3 - Nanoparticle Re-assembly on Surfactant Removal

Colloidal metallic or metal oxide nanoparticles self-assembled into regular arrays need to get rid off the surfactant shell for some applications. For example, the gas sensing function of metal oxide nanoparticles is

based on exposition of their surface to residual gases in ambient atmosphere to initiate chemical reactions. Here, the UV photolysis and ozonolysis proved to be efficient methods to remove the organic molecule chains bonded to the nanoparticle core [8]. On the other hand, the surfactant removal may result in distinct changes in the order of nanoparticle array due to a changed equilibrium between various forces governing the self-assembly such as van der Waals attraction, steric repulsion, electric or magnetic moments, or adhesion to the substrate [9]. Hence, the studies of UV/ozone driven re-assembly effects is a highly relevant issue.

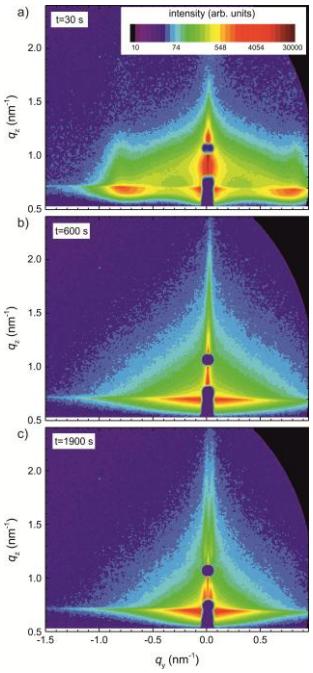

Fig. 9 – GISAXS pattern evolution during UV/ozone treatment

The *in situ* GISAXS measurements were performed simultaneously with the grazing-incidence wide-angle X-ray scattering (GIWAXS) measurements during a combined UV/ozone irradiation at BL23A beamline at NSRRC, Taiwan. While the GISAXS probes the nanoparticle re-arrangement, the GIWAXS gives insight into accompanying phase transitions at the atomic level inside the nanoparticles. The solution of the same colloidal Ag nanoparticles as those in the Example 2 was applied to deposit a self-assembled monolayer array on silicon by a modified Langmuir–Schaefer method [5]. Repeating this deposition, a vertically uncorrelated nanoparticle bilayer was prepared. A custom designed window-less UV reactor equipped with an ozone generating low pressure mercury lamp ($h\nu$=4.9 eV, 6.7 eV) and the total UV intensity at the sample surface of 2 mW/cm^2 was used.

The most prominent feature visible in the GISAXS pattern before the UV/ozone treatment are the two symmetrical Bragg rods corresponding to the in-plane correlations of nanoparticle positions in the self-assembled bilayer (Fig. 9a). Considering the nanoparticle diameter determined from SAXS and the interparticle distance determined from the Bragg rod position (see Example 2), the surfactant shell thickness of 1.2 nm was detemined. The Fig. 9b shows an intermediate state after 600 s. The Bragg rods visible at the early surfactant removal times disappeared completely and the reciprocal space map shows no signs of the in-plane nanoparticle position correlations. The Fig. 9c shows the final GISAXS reciprocal space map after 1900 s where new Bragg rods at $q_{y,1B} = \pm 0.026$ nm^{-1} (*i.e.* very close to the central line) are visible. These Bragg rods correspond to the mean lateral correlation length $\xi = 2\pi/q_{y,1B} \approx 240$ nm of the oxidized nanoparticle agglomerates (see further).

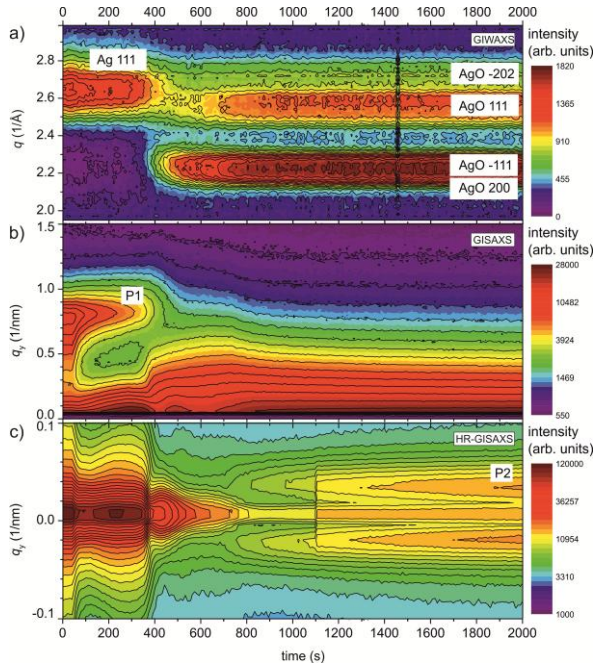

Fig. 10 – Temporal evolution of the selected cuts along q_y in the GISAXS pattern: (a) GIWAXS, (b) GISAXS, and (c) HR-GISAXS

To quantify the temporal evolution of the loss of the original nanoparticle self-assembly and the final nanoparticle agglomeration as well as the phase transition due to oxidation of the silver nanoparticles, specific areas in the GISAXS pattern were integrated and plotted as a function of the UV/ ozone treatment time. The Fig. 10a shows the temporal evolution of GIWAXS obtained by a pie-integration for q values 1.9-3.0 Å^{-1}. For the pristine sample, the Ag 111 diffraction is observed while on the UV/ozone treatment, the −202, 111, −111, 200 AgO diffractions appear. The Fig. 11a shows the integrated area under the Ag 111 and AgO −111 diffractions. The full width at half-maximum (FWHM) of the AgO −111 diffraction peak is shown in Fig. 11b along with the evaluated AgO unit cell volume. The Fig. 10b depicts the temporal evolution of the GISAXS pattern line cuts along q_y integrated between q_z values 0.675-0.725 nm^{-1}. The integrated area under the GISAXS P1 peak of the first Bragg rod stemming from the pristine nanoparticle position correlations in the self-assembled bilayer is shown in Fig. 11c and its maximum position and FWHM are plotted in Fig. 11d. Finally, Fig. 10c shows the temporal evolution of the GISAXS pattern line cuts along q_y integrated between q_z values 0.8-0.85 nm^{-1} labelled as high-resolution GISAXS (HR-GISAXS). The temporal evolution of the

integrated area under the P2 peak of the newly formed Bragg rod is shown in Fig. 11c and its maximum position and FWHM are plotted in Fig. 11d.

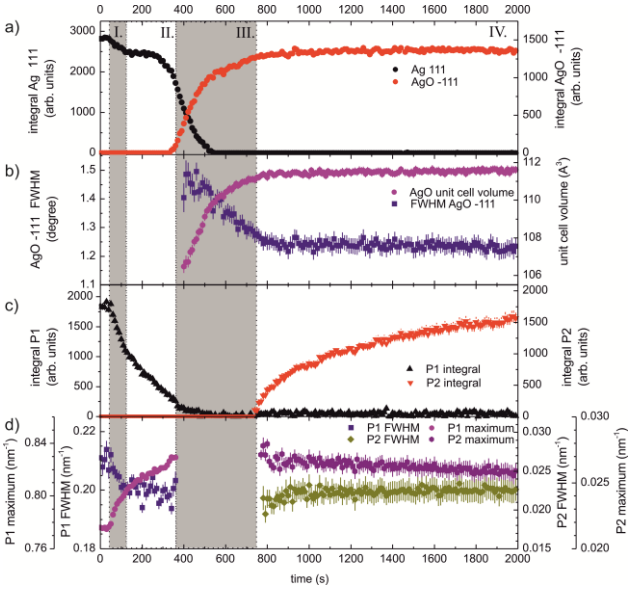

Fig. 11 – Temporal evolution of some selected parameters derived from the patterns in Figs. 9, 10

Relying on these results, we can distinguish four stages of the UV/ozone treatment (Fig. 11). In the stage I, a gradual decrease of the integrated area under the P1 Bragg peak implies a loss of the correlations in the self-assembled nanoparticle array due to the gradual removal of the surfactant molecules (Fig. 11c). The shift of the P1 Bragg peak toward higher q_y values suggests a mean interparticle spacing reduction and a nanoparticle array densification (Fig. 11d) that can be attributed to better filing up the voids in the bottom layer by the nanoparticles from the top one during the rearrangement. The FWHM narrowing of the P1 Bragg peak implies a locally enhanced nanoparticle correlation in the bottom layer (Fig. 11d). This evolution persists also in stage II which is characterized by further decay of the nanoparticle correlations, as evidenced by the decreasing integrated area under the P1 Bragg peak, and further reduction of the mean interparticle distance, as shown by the P1 Bragg peak shift toward higher q_y values) (Fig. 11c,d).

In the GIWAXS, a decrease of the integrated area under the Ag 111 diffraction is observed to the end of stage II and continues in stage III where the appearance of the AgO monoclinic phase due to the nanoparticle surface oxidation after the surfactant removal is detected and tracked by a strong −111 diffraction (Fig. 11a). The oxidation is completed to the end of stage III. The growth of the AgO phase in the nanoparticle volume is accompanied by a FWHM decrease of AgO −111 diffraction which suggests a more regular space lattice.

The GISAXS and HR-GISAXS patterns do not exhibit any Bragg rods in stage III (Fig. 10b,c) indicating the absence of any nanoparticle position correlations. The appearance of the P2 peak at low q_y in stage IV (Fig. 10c) implies a self-assembly of AgO nanoparticles into large nanoparticle aggregates which continues even after 2000 s UV/ozone tretment as the P2 peak integral intensity does not come to saturation (Fig. 11c). The FWHM of P2 peak is constant during the nanoparticle agglomeration phase (Fig. 11d) which indicates a stable lateral correlation length during the agglomeration process.

These results confirm importance of the detailed knowledge of the nanoparticle surfactant removal by UV/ozone treatment for preparation of advanced gas sensors based on metal oxide nanoparticles.

AKNOWLEDGEMENTS

The work was supported by the Slovak Research and Development Agency, project No. APVV-0308-11, grant agency VEGA Bratislava, project no. 2/0004/15, M-ERA-Net XOPTICS project and COST Actions MP1203 and MP1207.

REFERENCES

1. G. Renaud, R. Lazari, C. Revenant, A. Barbier, M. Noblet, O. Urlich, F. Leroy, J. Jupille, Y. Borenzstein, C.R. Henry, J.P. Deville, F. Scheurer, J. Mane-Mane, O. Fruchart, *Science* **300**, 1416 (2003).
2. P. Müller-Buschbaum, E. Bauer, E. Maurer, S.V. Roth, R. Gehrke, M. Burghammer, C. Riekel, *J. Appl. Cryst.* **40**, s341 (2007).
3. G. Renaud, R. Lazzari, F. Leroy, *Surf. Sci. Rep.* **64**, 255 (2009).
4. D.V. Talapin, E.V. Shevchenko, M.I. Bodnarchuk, X.C. Ye, J. Chen, C.B. Murray, *Nature* **461**, 964 (2009).
5. K. Végsö, P. Šiffalovič, M. Benkovičová, M. Jergel, Š. Luby, E. Majková, I. Capek, T. Kocsis, J. Perlich, S.V. Roth, *Nanotechnology* **23**, 045704 (2012).
6. M. Fukuto, R.K. Heilmann, P.S. Pershan, A. Badia, R.B. Lennox, *J. Chem. Phys.* **120**, 3446 (2004).
7. R. Lazzari, in *X-ray and Neutron Reflectivity*, edited by J. Daillant, A Gibaud (Berlin-Heidelberg: Springer, 2009), 283.
8. J. Park, A.L. Gomez, M.L. Walser, A. Lin, S.A. Nizkorodov, *Phys. Chem. Chem. Phys.* **8**, 2506 (2006).
9. P. Šiffalovič, L. Chitu, E. Majková, K. Végsö, M. Jergel, Š. Luby, I. Capek, A. Šatka, G.A. Maier, J. Kečkeš, A. Timmann, S.V. Roth, *Langmuir* **26**, 5451 (2010).